1-1-2020

An In-Depth Study of Zn Metal Surface Chemistry for Advanced Aqueous Zn-Ion Batteries

Junnan Hao
University of Wollongong, jh845@uowmail.edu.au

Bo Li

Xiaolong Li
University of Wollongong

Xiaohui Zeng
University of Wollongong, xz990@uowmail.edu.au

Shilin Zhang
sz384@uowmail.edu.au

See next page for additional authors

An In-Depth Study of Zn Metal Surface Chemistry for Advanced Aqueous Zn-Ion Batteries

Abstract

© 2020 WILEY-VCH Verlag GmbH & Co. KGaA, Weinheim Although Zn metal has been regarded as the most promising anode for aqueous batteries, it persistently suffers from serious side reactions and dendrite growth in mild electrolyte. Spontaneous Zn corrosion and hydrogen evolution damage the shelf life and calendar life of Zn-based batteries, severely affecting their industrial applications. Herein, a robust and homogeneous ZnS interphase is built in situ on the Zn surface by a vapor–solid strategy to enhance Zn reversibility. The thickness of the ZnS film is controlled via the treatment temperature, and the performance of the protected Zn electrode is optimized. The dense ZnS artificial layer obtained at 350 °C not only suppresses Zn corrosion by forming a physical barrier on the Zn surface, but also inhibits dendrite growth via guiding the Zn plating/stripping underneath the artificial layer. Accordingly, a side reaction-free and dendrite-free Zn electrode is developed, the effectiveness of which is also convincing in a MnO2/ZnS@Zn full-cell with 87.6% capacity retention after 2500 cycles.

Disciplines

Engineering | Physical Sciences and Mathematics

Publication Details

Hao, J., Li, B., Li, X., Zeng, X., Zhang, S., Yang, F., Liu, S., Li, D., Wu, C. & Guo, Z. (2020). An In-Depth Study of Zn Metal Surface Chemistry for Advanced Aqueous Zn-Ion Batteries. Advanced Materials,

Authors

Junnan Hao, Bo Li, Xiaolong Li, Xiaohui Zeng, Shilin Zhang, Fuhua Yang, Sailin Liu, Dan Li, Chao Wu, and Zaiping Guo

An in-depth study of Zn metal surface chemistry for advanced aqueous Zn-ion batteries

*Junnan Hao, Bo Li, Xiaolong Li, Xiaohui Zeng, Shilin Zhang, Fuhua Yang, Sailin Liu, Dan Li, Chao Wu, Zaiping Guo**

J. Hao, X. Li, X. Zeng, S. Zhang, F. Yang, S. Liu, Dr. Chao Wu, Prof. Z. Guo
Institute for Superconducting and Electronic Materials, Australian Institute for Innovative Materials, University of Wollongong, Wollongong, NSW 2522, Australia
E-mail: zguo@uow.edu.au
J. Hao, Prof. Z. Guo
School of Mechanical Materials, Mechatronics & Biomedical Engineering, University of Wollongong, Wollongong, NSW 2500, Australia
Dr. B. Li
School of Chemistry and Environment, South China Normal University, Guangzhou 510006, People's Republic of China
Dr. D. Li
College of Chemistry, Zhengzhou University, Zhengzhou 450001, China

Keywords: Zn ion batteries, Zn anode protection, in situ strategy, side reactions, DFT calculation

Although Zn metal has been regarded as the most promising anode for aqueous batteries, it persistently suffers from serious side reactions and dendrite growth in mild electrolyte. The spontaneous Zn corrosion and hydrogen evolution damage the shelf life and calendar life of Zn-based batteries, severely affecting their industrial applications. Herein, a robust and homogeneous ZnS interphase is built in situ on the Zn surface by a vapour-solid strategy to enhance Zn reversibility. The thickness of the ZnS film is controlled via the treatment temperature, and the performance of the protected Zn electrode is optimized. The dense ZnS artificial layer obtained at 350 °C not only suppresses Zn corrosion by forming a physical barrier on the Zn surface, but also inhibits dendrite growth via guiding the Zn plating/stripping underneath the artificial layer. Accordingly, a side reaction-free and dendrite-free Zn electrode is developed, the effectiveness of which is also convincing in a MnO_2/ZnS@Zn full-cell with 87.6% capacity retention after 2500 cycles.

1. Introduction

Recently, Zn metal batteries have gained extensive attention due to the advantages of Zn metal stemming from its high abundance, low toxicity, low reduction potential, high hydrogen evolution over-potential, and high theoretical capacity (gravimetric capacity of 820 mA h g^{-1} and volumetric capacity of 5855 mA h cm^{-3}).[1] Nevertheless, Zn metal anode in mild electrolyte still faces severe inherent problems of dendrite growth, Zn corrosion, and hydrogen evolution, which significantly compromise the Coulombic efficiency (CE), cycling stability, and practical implementation of Zn metal batteries.[2]

According to our previous study,[3] fresh Zn metal is highly unstable in mild electrolyte and generates a loose $Zn_4SO_4(OH)_6{\cdot}xH_2O$ layer that cannot block the electrolyte to stop side reactions, including the hydrogen evolution, which easily causes battery swelling. It is well-known that there is a dense $Zn_5(CO_3)_2(OH)_6$ passivation layer on the Zn metal surface due to its oxidation by contact with oxygen and moisture in the air.[4] This layer is homogeneous and dense enough to effectively reduce the Zn corrosion rate in air.[5] Could this layer protect the fresh Zn in mild electrolyte by termination of side reactions? Does the existence of this layer have an impact on the Zn stripping/plating behavior during Zn battery operation? Up until now, little attention has been paid to in depth understand this dense passivation film in Zn metal batteries.

To date, most efforts have been spent on suppressing Zn dendrite growth to enhance the CE of Zn metal, such as by designing eutectic Zn-alloys,[6] developing new/highly-concentrated electrolytes,[1a, 7] introducing different electrolyte additives,[8] and controlling the Zn deposition.[9] Although these strategies stabilize Zn metal to some extent, the battery performance is still far from satisfactory for industrial application due to the persistence of side reactions.[10] Because Zn electrode continuously reacts with the electrolyte during transportation and during the shelf time after battery assembly but before customer use, the practical application of Zn batteries is severely limited. Building artificial solid-electrolyte interphase (SEI) layers should be a good alternative, which could not only inhibit Zn dendrite

growth, but also stop the side reactions.[11] The inhomogeneous and uncompacted artificial layers built by ex situ techniques, however, are unlikely to effectively block electrolyte from the Zn metal surface, and thus the side reactions, including Zn corrosion and hydrogen evolution, would still occur when the uncovered Zn contacted with the electrolyte. Even worse, such SEI layers feature poor adhesion and are easily detached from the Zn surface due to the volume changes during cycling, so they cannot fully protect the fresh Zn metal underneath. Moreover, most artificial layers still suffer from low transference numbers ($t_{Zn^{2+}}$), which may negate the benefits of the inhibition of dendrite growth. Because the divalent Zn^{2+} ion (radius, 0.74 Å) has a much higher electric charge density compared to the monovalent Li^+ and Na^+ ions (radii, 0.76 and 1.02 Å, respectively)[12], a huge energy barrier is created for Zn^{2+} transfer in these artificial layers. Therefore, in situ development of a dense and homogeneous artificial SEI with strong adhesion and a high $t_{Zn^{2+}}$ is still challenging for Zn metal anode.

Here, the protective function of the oxidation layer on Zn metal is studied in-depth in 1 M $ZnSO_4$ electrolyte, with the results indicating that this dense $Zn_5(CO_3)_2(OH)_6$ oxidation layer is thermodynamically unstable in mild electrolyte and cannot act as an effective barrier against Zn corrosion. Since it would be gradually transformed into a loose $Zn_4SO_4(OH)_6{\cdot}xH_2O$ layer after soaking in 1 M $ZnSO_4$ electrolyte. To effectively suppress the Zn dendrite growth and the side reactions, we have elaborately built a compact artificial ZnS layer on the Zn metal surface by an in situ vapour-solid strategy. Different temperatures have been conducted, with the results suggesting that a homogeneous ZnS coating was realized at 350 °C (ZnS@Zn-350). At the interphase of ZnS and Zn metal, S atoms have a bonding interaction with the Zn atoms in the Zn metal due to the occurrence of charge migration, as confirmed by the density functional theory (DFT) calculations. The unbalanced charge distribution not only enhances the Zn^{2+} diffusion at the ZnS@Zn interphase but also increases the adhesion of the ZnS film to the Zn surface. Importantly, the ZnS layer is highly stable in aqueous electrolyte, contributing to enhancement of the Zn reversibility by avoiding the side reactions. Thanks to its good

mechanical strength and high ionic conductivity, the ZnS coating film facilitates dendrite-free Zn plating/stripping, as confirmed by in situ optical microscopy. With this strategy, high cycling stability (> 2500 cycles) and high CE (> 99.8%) were realized in both symmetric cells and full-cells when coupled with MnO_2 cathode.

2. Results and discussion

2.1 Fundamental study on Zn metal

A dense zinc hydroxycarbonate (i.e. $Zn_5(CO_3)_2(OH)_6$ or $Zn_4CO_3(OH)_6{\cdot}H_2O$) passivation layer forms on the Zn metal surface once it is exposed to air, which can significantly retard the corrosion process by keeping out moisture and oxygen.[13] Can this passivation film protect the Zn metal or influence the Zn plating/stripping behavior in 1 M $ZnSO_4$ electrolyte? These fundamental issues are still unclear. To address these problems, the stability of this oxidation layer was first studied in 1 M $ZnSO_4$. A scanning electron microscope (SEM) image of bare Zn metal without polishing shows a flat surface with some holes (**Figure 1a**). After deep cleaning, the oxidation layer was removed, with many scratches remaining on the polished Zn metal (Figure S1, Supporting Information), which was confirmed by Fourier transform infrared (FTIR) spectroscopy (Figure S2, Supporting Information). Bare Zn foil shows an absorption at approximately 1500 cm^{-1}, corresponding to the v_3 $(CO_3)^{2-}$ antisymmetric stretching mode, which is convincing evidence of the presence of a $Zn_5(CO_3)_2(OH)_6$ layer.[14] No obvious absorption can be observed after polishing, indicating that the $Zn_5(CO_3)_2(OH)_6$ layer was thoroughly removed. Both the bare Zn metal and the polished Zn were soaked in 1 M $ZnSO_4$ electrolyte. After one week, the surfaces of both the bare and polished Zn metal incurred a severe corrosion reaction with significant colour change (Figure S3, Supporting Information). The SEM image in Figure 1b shows by-products with the morphology of regular hexagonal flakes that cover the whole surface of the bare Zn, which is similar to what is seen on the polished Zn (Figure S4, Supporting Information), demonstrating that the $Zn_5(CO_3)_2(OH)_6$ layer is highly active in the electrolyte. X-ray diffraction (XRD, Figure S5, Supporting Information)

and FTIR measurements were conducted to identify the by-products of both samples. The results indicated that the by-product generated on both electrodes was $Zn_4SO_4(OH)_6{\cdot}xH_2O$, as further confirmed by the energy dispersive spectroscopy (EDS) mapping of S and Zn elements (Figure 1c-e). Accordingly, the $Zn_5(CO_3)_2(OH)_6$ passivation layer cannot function as a protective layer in the electrolyte due to its high thermodynamic activity. The corrosion reaction of bare Zn with a $Zn_5(CO_3)_2(OH)_6$ passivation layer can be expressed as following:

$$Zn_5(CO_3)_2(OH)_6 + SO_4^{2-} + 4\,H^+ + (x-2)H_2O \rightarrow Zn_4SO_4(OH)_6 \cdot xH_2O + 2CO_2 + Zn^{2+} \quad (1)$$

$$Zn \leftrightarrow Zn^{2+} + 2e^- \quad (2)$$

$$2H_2O + 2e^- \leftrightarrow 2OH^- + H_2 \quad (3)$$

$$4Zn^{2+} + 6OH^- + SO_4^{2-} + xH_2O \leftrightarrow Zn_4SO_4(OH)_6 \cdot xH_2O \quad (4)$$

The electrochemical performance of symmetrical Zn cells with/without polishing was tested to investigate the influence of the $Zn_5(CO_3)_2(OH)_6$ layer on the Zn electrodeposition behaviour. Figure 1f compares the initial charge/discharge voltage profiles of both cells. Remarkably, the bare Zn cell displays a higher voltage hysteresis compared to the polished Zn cell at the start of charge, indicating its higher energy barrier for Zn stripping/plating due to the passivation layer.[15] As the charge proceeds, the voltage hysteresis of the bare Zn cell decreases, probably due to the dissolution of the passivation layer in $ZnSO_4$ electrolyte, but it increases in the polished Zn cell, indicating the enhanced impedance due to the by-product layer formation. Electrochemical impedance spectroscopy (EIS) measurements of Zn cells were conducted after different numbers of cycles (Figure S6, Supporting Information). Both bare and polished Zn cells show two different charge transfer steps after one cycle and after 50 cycles, manifesting the additional by-product layer generated during the charge-discharge process. Digital images of the bare and polished Zn metal electrodes reveal that the two kinds of Zn electrodes suffered from serious surface corrosion with an obvious colour change during cycling (Figure S7, Supporting Information). SEM images show by-product formation and corrosion on the Zn surface regardless of the presence of a passivation layer (Figure S8, Supporting Information),

as further confirmed by the XRD patterns. Before cycling, only the characteristic peaks of Zn metal located at 36.4°, 39.1°, and 43.3° can be found for the bare Zn electrode (Figure 1g), which suggests that the $Zn_5(CO_3)_2(OH)_6$ layer is hard to identify.[16] After one cycle, a small peak at 8.5° can be detected, corresponding to the (002) planes of $Zn_4SO_4(OH)_6{\cdot}xH_2O$ by-product, and the intensity increases with further cycling (50 cycles), indicating the aggravated side reactions during battery operation, which is similar to the XRD patterns of the polished Zn after different numbers of cycles (Figure S9, Supporting Information). Although removal of the $Zn_5(CO_3)_2(OH)_6$ reduces the energy barrier for Zn stripping/plating and prolongs the cycling lifespan from ~100 h to ~250 h at 2 mA cm^{-2} (Figure S10, Supporting Information), the performance of the polished Zn cell is still far from satisfactory due to the notorious Zn dendrite growth and side reactions.

2.2 In situ building ZnS film

Building a dense and homogeneous SEI layer is an effective strategy to enhance the Zn reversibility.[17] Based on the phase diagram of sulfur (Figure S11, Supporting Information), we have elaborately grown an artificial ZnS film on the Zn metal surface by an in situ vapour-solid reaction, as illustrated in **Figure 2a**. Specifically, sulfur can be vaporized at ~200 °C under the pressure of ~1×10^{-3} atm, and the sulfur vapour will react with Zn metal by generating ZnS at high temperatures. Accordingly, Zn foil was put in a specially designed tube with 100 g sulfur powder below it. Then, the tube was evacuated and sealed. At high temperature, the gaseous sulfur vapour spread to the Zn metal surface and reacted with Zn metal to generate a dense and uniform ZnS layer. As aforementioned, Zn electrode, whether with/without a $Zn_5(CO_3)_2(OH)_6$ layer, is highly unstable, and suffers from side reactions and dendrite growth during battery operation (Figure 2b), which not only fades the CE and reversible capacity, but also shortens the cycling lifespan of Zn batteries. In striking contrast, the ZnS protective layer on the Zn surface not only effectively inhibits the corrosion reactions by blocking the electrolyte, but also

suppresses the Zn dendrite growth by guiding the Zn^{2+} stripping/plating underneath, enhancing the reversibility of Zn metal (Figure 2b).

To study the influence of the treatment temperature on the ZnS film, different operating temperatures of 300, 350, and 400 °C were conducted. From the XRD patterns of ZnS@Zn electrodes (**Figure 3a**), the sample obtained at 300 °C (ZnS@Zn-300) only shows the characteristic peaks of Zn metal, indicating no obvious formation of ZnS film at this temperature, as further confirmed by EDS mapping (Figure S12, Supporting Information). No clear S element layer can be found on the Zn metal surface, suggesting that this is an improper operating temperature. When the temperature was increased to 350 °C, the XRD pattern displayed new peaks at 28.6°, 47.5°, and 56.3°, corresponding to the (111), (220), and (311) planes of ZnS (PDF # 00-005-0566), respectively.[18] The intensity of these peaks increased when the temperature was increased to 400 °C. Figure S13 (Supporting Information) presents digital images of ZnS@Zn electrodes obtained at different temperatures, with the ZnS@Zn-300 foil showing almost no change in colours or luminosity. Remarkably, the surfaces of the ZnS@Zn-350 and ZnS@Zn-400 foils changed significantly due to the sulfur-vapour reaction. Unfortunately, the ZnS@Zn-400 foil also suffered from serious distortion due to the deformation of the Zn metal at the high temperature, indicating that the high temperature of 400 °C is unsuitable, too. SEM images show that the Zn surface was evenly covered by ZnS at 350 °C (Figure 3b). The cross-sectional image (Figure 3c) reveals a homogeneous ZnS coating layer with a thickness of ~0.5 μm, as further confirmed by the high-resolution image (Figure S14, Supporting Information) and EDS mapping (Figure 3d). X-ray photoelectron spectroscopy (XPS) spectra of bare Zn and ZnS@Zn-350 were collected (Figure 3e, f), and the bare Zn electrode only shows the binding energies of Zn $2p_{1/2}$ and Zn $2p_{3/2}$ at 1045.1 and 1021.9 eV, respectively. Whereas, the ZnS@Zn-350 displays the S signals of S $2p_{3/2}$ and S$2p_{1/2}$ located at 161.9 and 163.2 eV, respectively.[19] Importantly, a small binding energy shift in the Zn $2p_{3/2}$ region was mainly due to the formation of Zn-S polar bonds at the interphase of ZnS and Zn

metal, which enhances the adhesion of the ZnS film to the Zn metal. According to a previous report,[20] the Zn (002) facet is transformed into ZnS (002) at the interphase of ZnS@Zn, as illustrated in Figure 3g. DFT calculations revealed that the bonding interaction occurs between the S atoms and Zn atoms in the Zn metal, which modifies the charge distribution (Figure 3h) and further leads to an unbalanced charge distribution at the interphase (Figure 3i). The unbalanced charge distribution not only accelerates the Zn^{2+} diffusion at the ZnS@Zn interphase, but also enhances the adhesion of the ZnS layer to the Zn metal.[21] Rolling and twisting experiments were also conducted to evaluate the adhesion between the ZnS layer and the Zn metal. As depicted in Figure S15 (Supporting Information), the ZnS@Zn-350 foil keeps its surface integrity after twisting to various degrees, suggesting good adhesion between the ZnS layer and the Zn metal.

2.3 Blocking electrolyte and suppressing dendrite growth

In order to study the stability of the ZnS layer, ZnS@Zn-350 foil was soaked in 1 M $ZnSO_4$ electrolyte for 10 days. The digital images of the ZnS@Zn-350 foil show similar surfaces before and after soaking in electrolyte for 10 days (Figure S16, Supporting Information), demonstrating that this layer is highly stable. The XRD pattern was collected after the soaking in electrolyte (Figure S17, Supporting Information), which is similar to that for ZnS@Zn-350 foil before soaking and without any peaks for the $Zn_4SO_4(OH)_6{\cdot}xH_2O$ by-product, indicating that the side reactions between the Zn metal and the electrolyte were disrupted. The impact of the ZnS layer on Zn metal corrosion was investigated by linear polarization experiments in 1 M $ZnSO_4$ electrolyte (Figure S18, Supporting Information). Compared to the bare Zn, the corrosion potential of the ZnS@Zn-350 increased from −1.052 V to −1.048 V, suggesting that it has less tendency towards corrosion reactions.[22] Notably, this ZnS layer also reduces the corrosion current by 368.5 μA cm^{-2}. In addition to inhibiting the side reactions, the ZnS layer also functions as a robust artificial SEI to suppress Zn dendrite growth because it has poor electronic conductivity, but high ionic conductivity and high $t_{Zn^{2+}}$. It is well-known that cubic

ZnS has been widely used as a semiconductor due to its wide-band-gap properties.[23] The electrical resistivity (ρ) of the ZnS protective film was also evaluated (Figure S19, Supporting Information). According to the following formula $\rho = \frac{R*S}{L} = \frac{U*S}{I*L}$, in which R is the resistance, I is the applied current, L is the thickness of the ZnS, U is the corresponding voltage, and S is the contact area, ρ was estimated as ~1.5×10^5 Ω·cm ($\sigma \approx 6.5 \times 10^{-6}$ S·cm^{-1}). The high resistance introduced by the insulating ZnS layer is critical for establishing the necessary potential gradient across the artificial film to drive Zn^{2+} diffusion through the layer.[24] In addition, the ZnS film features good ionic conductivity (evaluated as ~1.3×10^{-5} S·cm^{-1}, Figure S20, Supporting Information), which facilitates Zn^{2+} diffusion through this protective film. Furthermore, the $t_{Zn^{2+}}$ was further calculated to quantitatively describe the Zn^{2+} conducting ability of the ZnS protective layer. In a bare Zn symmetric cell, a rather low $t_{Zn^{2+}}$ of 0.33 was obtained (Figure S21a, Supporting Information), which is mainly due to the strong preferential solvation of Zn^{2+} over the anions, leading to a bulky solvation shell around Zn^{2+}. SO_4^{2-} anions tend to migrate in the opposite direction from Zn^{2+} and eventually accumulate at the electrode surface, resulting in a build-up of the concentration gradient. This concentration gradient not only limits the rate at which the battery may be charged or discharged, but also creates a concentration overpotential that limits the operating voltage of the battery, thus limiting the power and energy density of the battery.[25] Notably, $t_{Zn^{2+}}$ can be dramatically improved to ~0.78 after introducing the ZnS layer (Figure S21b, Supporting Information), suggesting that the anions were effectively retarded by this protective layer.

To confirm the suppression of Zn dendrite growth by the ZnS artificial layer, transparent symmetric cells were assembled to in situ monitor the Zn plating/stripping behaviour using an optical microscope equipped with a digital camera. A high current density of 5 mA cm^{-2} with 10 min of intermittence was applied to repeatedly conduct plating/stripping measurements. **Figure 4a** presents images of a bare Zn electrode after different plating/stripping cycles. Before

cycling, the bare Zn electrode displays a smooth edge. After 50 cycles, protrusions start to grow along the edge of the bare Zn electrode, which evidences uneven Zn plating. These protrusions gradually turns into Zn dendrites on the Zn electrode with further cycling. In strong comparison, the ZnS@Zn-350 electrode exhibits smooth Zn plating and stripping in Figure 4b. There is still no sign of protrusions or Zn dendrite generation, even after 250 cycles.

SEM was further conducted to observe the Zn electrodeposition with/without the ZnS protective layer. Zn deposition was conducted under 1 mA cm^{-2} with the deposition capacity of 1 mA h cm^{-2} and 2 mA h cm^{-2}, respectively. Figure 4c shows a cross-sectional image of the bare Zn metal after Zn plating (1 mA h cm^{-2}). Remarkably, uneven deposition occurred on the Zn surface with serious agglomeration, which easily triggers dendrite growth. After deposition of 2 mA h cm^{-2}, the agglomeration was aggravated, raising a potential safety issue after further Zn plating (Figure 4d). In contrast, no obvious Zn plates or protrusions were generated on the ZnS@Zn-350 surface after 1 mA h cm^{-2} of plating (Figure 4e), indicating that the ZnS protective layer helps to guide homogeneous Zn deposition underneath the film. Moreover, the thickness of the deposited Zn was approximately 1.5 μm, similar to its theoretical value (~1.7 μm under 1 mA h cm^{-2}). Even after 2 mA h cm^{-2} of plating, uniform deposition under the ZnS layer was still observed, as shown in Figure 4f, resulting in dendrite-free Zn plating.

2.4 Electrochemical performance of ZnS@Zn electrode

The CE is one of the most important parameters used to evaluate the reversibility of Zn plating and stripping.[26] In a Cu-Zn cell, the CEs were calculated from the ratio of Zn removed from the Cu substrate to that deposited during the same cycle. The ZnS protective layer on Cu foil was obtained by the doctor blading method. First, the morphology of Zn deposition on the bare Cu and ZnS@Cu was studied at current density of 2 mA cm^{-2} with a capacity of 1 mA h cm^{-2}. Clearly, the bare Cu substrate was covered by mossy Zn plates with obvious protrusions. In comparison, no obvious protrusions were generated on the ZnS@Cu surface, further indicating that the ZnS protective layer guides the Zn deposition (Figure S22, Supporting Information). In

the Cu-Zn cell, the initial CE was only ~77.6% and gradually increased to ~97.6% after the first 20 cycles (Figure 4g). Such a CE is still low, however, due to the poor reversibility of Zn metal caused by the side reactions and dendrite formation. Notably, the CEs fluctuate greatly after ~120 cycles, which is mainly due to short-circuiting of the battery. The ZnS@Cu-Zn cell, however, displayed a much higher initial CE of ~88.5% compared to the Cu-Zn cell, and it increased to 99.2% in the following 10 cycles. Even after 200 cycles, the CE remained stable, mainly benefiting from the suppression of side reactions and dendrite growth. The charge-discharge voltage profiles for different cycles of the Cu-Zn cell are shown in Figure 4h. The initial voltage hysteresis is ~141 mV for the Cu-Zn cell, much higher than that for the ZnS@Cu-Zn cell (~105 mV, Figure 4i), indicating a higher energy barrier for Zn nucleation/dissolution in the phase transition between Zn^{2+} ions and Zn metal.[27]

The stability of Zn metal anode with/without a ZnS layer was evaluated by long-term galvanostatic cycling of the symmetrical cells (**Figure 5a**). After cycling for ~100 h at 2 mA cm^{-2}, a sudden reduction of the polarization voltage appeared in the bare Zn cell, which might be ascribed to a dynamic dendrite-induced short circuit. In contrast, the ZnS@Zn-350 cell displayed prolonged cycling stability for more than 1100 h. Figure 5b compares the first charge-discharge voltage profiles of both cells. The ZnS@Zn-350 cell delivers a polarization voltage of ~98 mV, much lower than that of the bare Zn cell (~153 mV), indicating its low energy barrier for Zn deposition. Even after 40 cycles, the bare Zn cell still maintains a large polarization voltage (Figure S23, Supporting Information). One of the probable reasons for the high energy barrier is that the accumulation of detrimental by-products may block the conduction of ions.[28] The rate performance of Zn cells was investigated at various current densities from 0.2 to 10 mA cm^{-2}, as shown in Figure 5c, in which the bare Zn cell always exhibits substantially higher voltage hysteresis than the ZnS@Zn-350 cell, suggesting low polarization and favourable stability in the ZnS@Zn-350 cell. After the rate tests, the morphology of the Zn and the ZnS@Zn-350 electrodes was studied by SEM. The bare Zn

electrode had an uneven surface with many agglomerated Zn plates, as shown in Figure S24 (Supporting Information), which is mainly caused by the Zn corrosion and dendrite growth. The ZnS@Zn-350 electrode displays a clean surface, however, resulting from its corrosion-free and dendrite-free stripping/plating behaviour (Figure S25, Supporting Information).

To further prove the suitability for application of ZnS@Zn-350 electrode, a MnO_2/Zn full-cell was assembled by choosing MnO_2 electrode as the cathode, since it is one of the most promising candidates for aqueous Zn batteries.[29] Figure S26 (Supporting Information) presents representative SEM images of electrodeposited MnO_2 on carbon cloth. The surface of the carbon cloth is covered by MnO_2 clusters featuring a petal-like nanostructure. The full-cell was tested in electrolyte consisting of 1 M $ZnSO_4$ + 0.1 M $MnSO_4$, in which $MnSO_4$ was used as an additive to inhibit the dissolution of Mn^{2+} from the MnO_2 cathode.[30] Typical stepwise charge-discharge curves of the MnO_2/ZnS@Zn-350 battery were observed at 1 C (Figure S27, Supporting Information), suggesting the Zn^{2+} and H^+ co-intercalation mechanism.[31] The cyclic voltammetry (CV) curves of the MnO_2/Zn and MnO_2/ZnS@Zn-350 batteries are compared in Figure S28 (Supporting Information) and Figure 5d. Clearly, the MnO_2/ZnS@Zn-350 battery shows smaller voltage polarization (~20 mV) than that of the MnO_2/Zn battery, indicating its good reversibility due to the ZnS protection. The long-term cycling stability curves of both batteries at the high rate of 5 C are plotted in Figure 5e. The cell with bare Zn foil presents an initial capacity of ~115.6 mA h g^{-1}. The capacity dramatically drops after 1000 cycles, however, mainly because the separator was pierced by Zn dendrites, leading to the short-circuiting of the battery. In contrast, the MnO_2/ZnS@Zn-350 battery delivers a higher initial capacity (125.8 mA h g^{-1}) compared to the MnO_2/Zn battery. After 2500 cycles, a high capacity of 110.2 mA h g^{-1} with a high CE of 99.3 % was retained, corresponding to capacity retention of 87.6%, which is mainly due to the inhibition of Zn corrosion and dendrite growth during the battery operation.

3. Conclusion

The protective function of $Zn_5(CO_3)_2(OH)_6$ passive film on Zn metal was explored in 1 M $ZnSO_4$ electrolyte. Although this dense passivation layer could passivate Zn metal in air by blocking oxygen and moisture, it cannot protect Zn metal in mild electrolyte. Accordingly, a homogeneous and dense ZnS protective film was introduced in situ on the Zn metal surface by a high-temperature vapour-solid strategy. This film was found to be highly stable in mild electrolyte, which contributes to improving the reversibility of Zn metal by avoiding the electrolyte-induced side reactions. Moreover, this robust ZnS film shows strong adhesion, good mechanical strength, and high ionic conductivity, which enables even Zn plating/stripping, as confirmed by in situ optical microscopy. The ZnS@Zn-350 symmetrical cell delivered a smaller voltage polarization and longer lifespan of > 1100 h at 2 mA h cm^{-1} compared to the bare Zn cells. Benefiting from the side-reaction-free and dendrite-free ZnS@Zn-350 electrode, the MnO_2/ZnS@Zn-350 full-cell displayed excellent cycling stability, with 87.6% capacity retention after 2500 cycles. Our fundamental findings offer a better understanding of Zn metal surface chemistry and pave the way to developing practical Zn metal batteries with mild electrolyte.

Supporting Information
Supporting Information is available from the Wiley Online Library or from the author.

Acknowledgements
Financial support provided by the Australian Research Council (ARC) (FT150100109, DP170102406, and DE190100504) is gratefully acknowledged. The authors thank the Electron Microscopy Centre (EMC) at the University of Wollongong. The authors also thank Dr. Tania Silver for her critical reading of this manuscript.

Conflict of Interest
The authors declare no conflict of interest.

Received: ((will be filled in by the editorial staff))
Revised: ((will be filled in by the editorial staff))
Published online: ((will be filled in by the editorial staff))

References

[1] a) F. Wang, O. Borodin, T. Gao, X. Fan, W. Sun, F. Han, A. Faraone, J. A. Dura, K. Xu, C. Wang, *Nat. Mater.* **2018**, *17*, 543-549; b) J. Fu, R. Liang, G. Liu, A. Yu, Z. Bai, L. Yang, Z. Chen, *Adv. Mater.* **2019**, *31*, 1805230; c) Y. Jin, L. Zou, L. Liu, M. H. Engelhard, R. L. Patel, Z. Nie, K. S. Han, Y. Shao, C. Wang, J. Zhu, *Adv. Mater.* **2019**, *31*, 1900567.

[2] a) B. Tang, L. Shan, S. Liang, J. Zhou, *Energy Environ. Sci.* **2019**, *12*, 3288-3304; b) M. Song, H. Tan, D. Chao, H. J. Fan, *Adv. Funct. Mater.* **2018**, *28*, 1802564; c) Q. Zhang, J. Luan, L. Fu, S. Wu, Y. Tang, X. Ji, H. Y. Wang, *Angew. Chem. Int. Ed.* **2019**, *58*, 15841-15847; d) M. Yan, P. He, Y. Chen, S. Wang, Q. Wei, K. Zhao, X. Xu, Q. An, Y. Shuang, Y. Shao, *Adv. Mater.* **2018**, *30*, 1703725.

[3] J. Hao, X. Li, S. Zhang, F. Yang, X. Zeng, S. Zhang, G. Bo, C. Wang, Z. Guo, *Adv. Funct. Mater.* **2020,** 2001263.

[4] P. K. Bowen, J. Drelich, J. Goldman, *Adv. Mater.* **2013**, *25*, 2577-2582.

[5] R. Ramanauskas, *Appl. Surf. Sci.* **1999**, *153*, 53-64.

[6] S. B. Wang, Q. Ran, R. Q. Yao, H. Shi, Z. Wen, M. Zhao, X. Y. Lang, Q. Jiang, *Nat. Commun.* **2020,** *11*, 1634..

[7] a) N. Zhang, F. Cheng, Y. Liu, Q. Zhao, K. Lei, C. Chen, X. Liu, J. Chen, *J. Am. Chem. Soc.* **2016**, *138*, 12894-12901; b) L. Zhang, I. A. Rodríguez-Pérez, H. Jiang, C. Zhang, D. P. Leonard, Q. Guo, W. Wang, S. Han, L. Wang, X. Ji, *Adv. Funct. Mater.* **2019**, *29*, 1902653; c) L. Ma, S. Chen, N. Li, Z. Liu, Z. Tang, J. A. Zapien, S. Chen, J. Fan, C. Zhi, *Adv. Mater.* **2020**, *32*, 1908121.

[8] a) S. J. Banik, R. Akolkar, *Electrochim. Acta* **2015**, *179*, 475-481; b) J. Hao, J. Long, B. Li, X. Li, S. Zhang, F. Yang, X. Zeng, Z. Yang, W. K. Pang, Z. Guo, *Adv. Funct. Mater.* **2019**, *29*, 1903605.

[9] a) J. Zheng, Q. Zhao, T. Tang, J. Yin, C. D. Quilty, G. D. Renderos, X. Liu, Y. Deng, L. Wang, D. C. Bock, *Science* **2019**, *366*, 645-648; b) Z. Wang, J. Huang, Z. Guo, X.

Dong, Y. Liu, Y. Wang, Y. Xia, *Joule* **2019**, *3*, 1289-1300; c) Q. Yang, G. Liang, Y. Guo, Z. Liu, B. Yan, D. Wang, Z. Huang, X. Li, J. Fan, C. Zhi, *Adv. Mater.* **2019**, *31*, 1903778.

[10] Y. Zeng, X. Zhang, R. Qin, X. Liu, P. Fang, D. Zheng, Y. Tong, X. Lu, *Adv. Mater.* **2019**, *31*, 1903675.

[11] a) Q. Yang, Y. Guo, B. Yan, C. Wang, Z. Liu, Z. Huang, Y. Wang, Y. Li, H. Li, L. Song, J. Fan, C. Zhi, *Adv. Mater.* **2020**, 2001755; b) K. Zhao, C. Wang, Y. Yu, M. Yan, Q. Wei, P. He, Y. Dong, Z. Zhang, X. Wang, L. Mai, *Adv. Mater. Interfaces* **2018**, *5*, 1800848; c) Z. Wang, J. Hu, L. Han, Z. Wang, H. Wang, Q. Zhao, J. Liu, F. Pan, *Nano Energy* **2019**, *56*, 92-99.

[12] J. Huang, Z. Guo, Y. Ma, D. Bin, Y. Wang, Y. Xia, *Small Methods* **2019**, *3*, 1800272.

[13] N. S. Sangaj, V. Malshe, *Prog. Org. Coat.* **2004**, *50*, 28-39.

[14] J. Winiarski, W. Tylus, K. Winiarska, I. Szczygieł, B. Szczygieł, *J. Spectrosc.* **2018**, *2018*, 14.

[15] R. Xu, X. Q. Zhang, X. B. Cheng, H. J. Peng, C. Z. Zhao, C. Yan, J. Q. Huang, *Adv. Funct. Mater.* **2018**, *28*, 1705838.

[16] Z. Liu, T. Cui, G. Pulletikurthi, A. Lahiri, T. Carstens, M. Olschewski, F. Endres, *Angew. Chem. Int. Ed.* **2016**, *55*, 2889-2893.

[17] S. S. Shinde, C. H. Lee, A. Sami, D. H. Kim, S. U. Lee, J. H. Lee, *ACS Nano* **2016**, *11*, 347-357.

[18] T. Zscheckel, W. Wisniewski, C. Rüssel, *Adv. Funct. Mater.* **2012**, *22*, 4969-4974.

[19] H. Borchert, S. Haubold, M. Haase, H. Weller, C. McGinley, M. Riedler, T. Möller, *Nano Lett.* **2002**, *2*, 151-154.

[20] Q. Li, C. Wang, *Appl. Phys. Lett.* **2003**, *82*, 1398-1400.

[21] a) J. Hao, J. Zhang, G. Xia, Y. Liu, Y. Zheng, W. Zhang, Y. Tang, W. K. Pang, Z. Guo, *ACS Nano* **2018**, *12*, 10430-10438; b). J. Hao, F. Yang, S. Zhang, H. He, G. Xia, Y. Liu,

C. Didier, T. Liu, W. K. Pang, V. K. Peterson, *Proc. Natl. Acad. Sci. U.S.A.* **2020**, *117*, 2815-2823.

[22] a) E. McCafferty, *J. Electrochem. Soc.* **1977**, *124*, 1869-1878; b) S. Hosseini, A. Abbasi, L. O. Uginet, N. Haustraete, S. Praserthdam, T. Yonezawa, S. Kheawhom, *Sci. Rep.* **2019**, *9*, 1-12.

[23] X. Xu, S. Li, J. Chen, S. Cai, Z. Long, X. Fang, *Adv. Funct. Mater.* **2018**, *28*, 1802029.

[24] X. Liang, Q. Pang, I. R. Kochetkov, M. S. Sempere, H. Huang, X. Sun, L. F. Nazar, *Nat. Energy* **2017**, *2*, 17119.

[25] R. Xu, Y. Xiao, R. Zhang, X. B. Cheng, C. Z. Zhao, X. Q. Zhang, C. Yan, Q. Zhang, J. Q. Huang, *Adv. Mater.* **2019**, *31*, 1808392.

[26] F. Wang, E. Hu, W. Sun, T. Gao, X. Ji, X. Fan, F. Han, X. Q. Yang, K. Xu, C. Wang, *Energy Environ. Sci.* **2018**, *11*, 3168-3175.

[27] Q. Yang, F. Mo, Z. Liu, L. Ma, X. Li, D. Fang, S. Chen, S. Zhang, C. Zhi, *Adv. Mater.* **2019**, *31*, 1901521.

[28] Z. Zhao, J. Zhao, Z. Hu, J. Li, J. Li, Y. Zhang, C. Wang, G. Cui, *Energy Environ. Sci.* **2019**, *12*, 1938-1949.

[29] a) D. Chao, W. Zhou, C. Ye, Q. Zhang, Y. Chen, L. Gu, K. Davey, S. Z. Qiao, *Angew. Chem. Int. Ed.* **2019**, *58*, 7823-7828; b) X. Zeng, J. Hao, Z. Wang, J. Mao, Z. Guo, *Energy Storage Mater.* **2019**, *20*, 410-437.

[30] Y. Zeng, X. Zhang, Y. Meng, M. Yu, J. Yi, Y. Wu, X. Lu, Y. Tong, *Adv. Mater.* **2017**, *29*, 1700274.

[31] W. Sun, F. Wang, S. Hou, C. Yang, X. Fan, Z. Ma, T. Gao, F. Han, R. Hu, M. Zhu, *J. Am. Chem. Soc.* **2017**, *139*, 9775-9778.

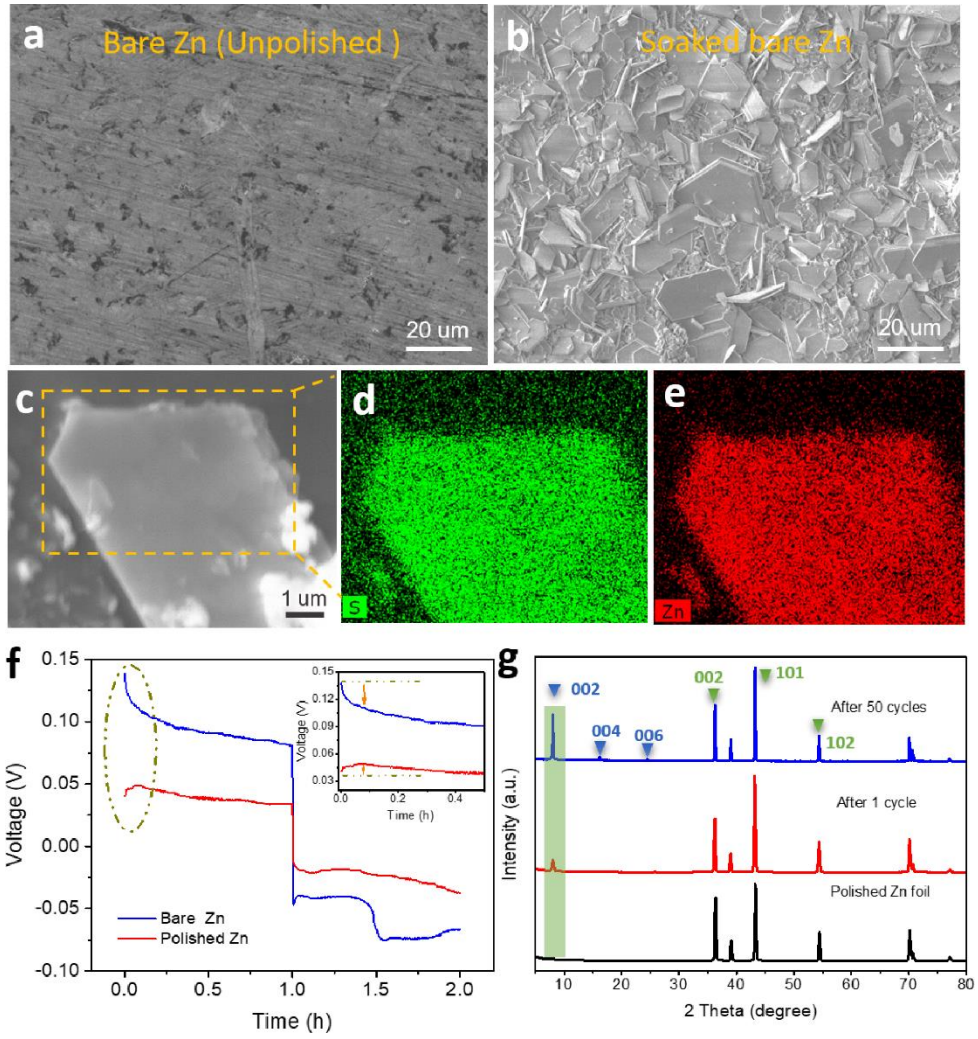

Figure 1. Characterization of the passivation layer on Zn metal. a) SEM image of bare Zn foil without polishing. b) SEM image of bare Zn foil after soaking in electrolyte for one week. c-e) Energy dispersive spectroscopy (EDS) mapping of the plates generated during the side reactions, showing the uniform distribution of S and Zn elements. f) Initial charge/discharge voltage profiles of a bare Zn symmetric cell and a polished Zn symmetric cell, with an enlargement in the inset. g) X-ray diffraction (XRD) patterns of bare Zn electrode before cycling, and after 1 and 50 cycles. Green peaks indicate metallic Zn and blue peaks indicate the by-product of $Zn_4SO_4(OH)_6{\cdot}xH_2O$.

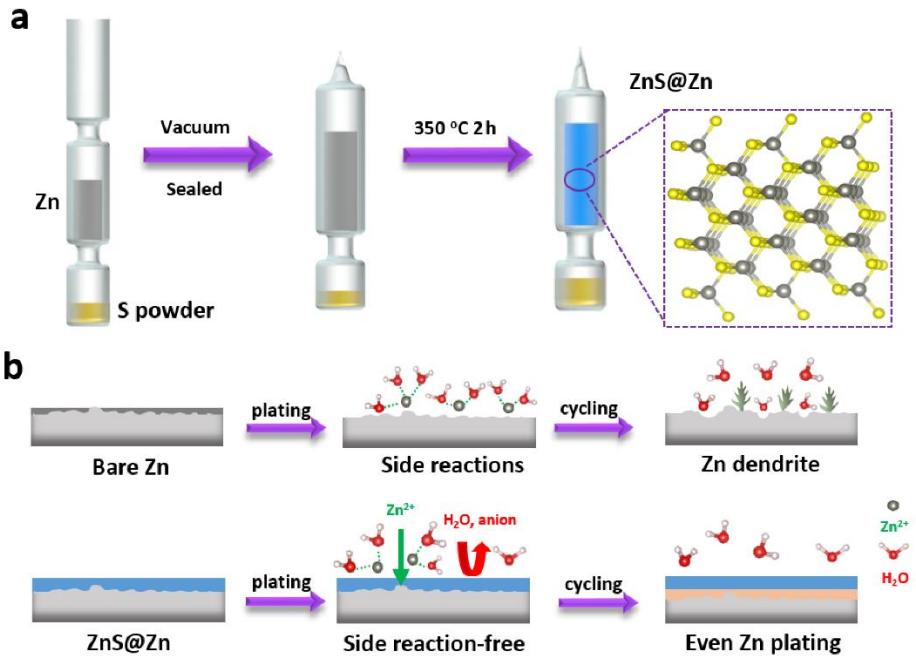

Figure 2. Schematic illustration of the artificial ZnS layer and Zn plating behaviour with/without ZnS. a) Introducing the ZnS layer on the surface of Zn metal substrate by an in situ strategy. b) Zn plating on the bare Zn foil with a $Zn_5(CO_3)_2(OH)_6$ passivation layer, leading to side reactions and dendritic Zn deposition. b) After incorporating the artificial ZnS layer on the Zn surface, uniform and compact Zn plating behaviour without side reactions can be obtained.

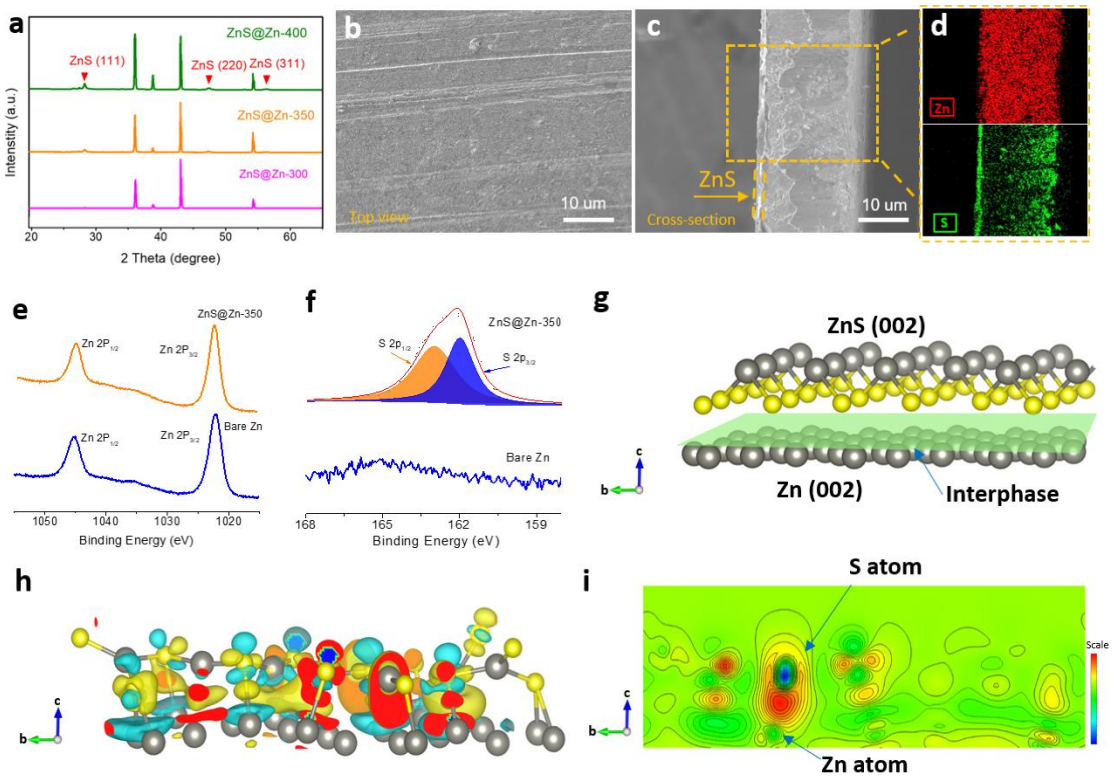

Figure 3. Characterization of Zn foil protected by a ZnS layer and the charge density distribution at the interface between the ZnS layer and the Zn metal. a) XRD patterns of ZnS@Zn foils obtained at different temperatures. b) SEM image of ZnS@Zn-350 foil (top-view). c) Cross-sectional image of ZnS@Zn-350 foil, showing that the thickness of the ZnS is approximately 0.5 µm. d) EDS mapping of Zn element (top) and S element (bottom). XPS characterizations of bare Zn and ZnS@Zn-350 foil: e) Zn 2p spectra, f) S 2p spectra. g) Schematic representation of the ZnS@Zn interphase of the ZnS@Zn-350 electrode. h) Electron density difference map at the ZnS@Zn interphase. i) Slice of the electron density difference map to show the unbalanced charge distribution.

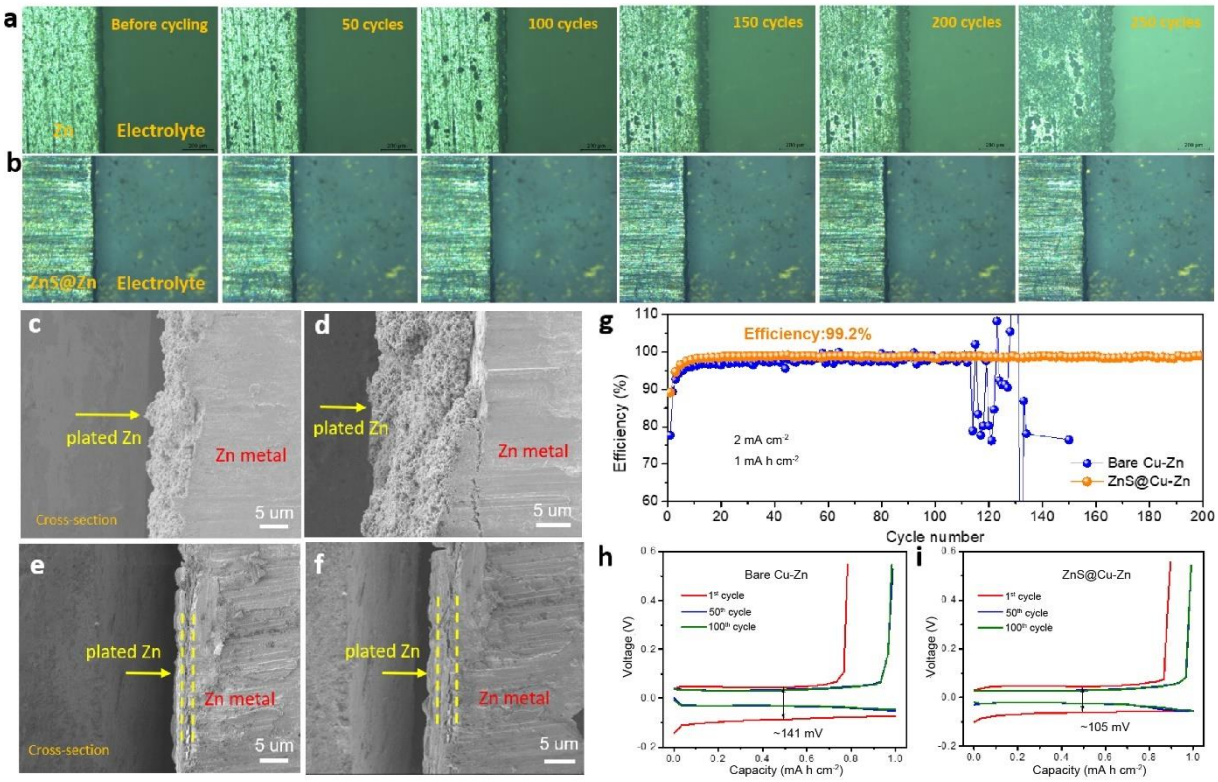

Figure 4. Optical microscopy and SEM studies of Zn plating behavior: a) Images of the front surface of bare Zn, and b) of ZnS@Zn-350 electrode in a symmetric transparent cell after the specified numbers of plating/stripping cycles. Cross-sectional SEM images of Zn deposition: c) on bare Zn metal at 1 mA cm^{-2} for areal capacity of 1 mA h cm^{-2}, d) 1 mA cm^{-2} for 2 mA h cm^{-2}, e) on ZnS@Zn-350 foil at 1 mA cm^{-2} for 1 mA h cm^{-2}, f) 1 mA cm^{-2} for 2 mA h cm^{-2}. g) CEs of Zn plating/stripping in bare Cu-Zn and ZnS@Cu-Zn cells with capacity of 1 mA h cm^{-2}. Voltage profiles of the bare Cu-Zn cell (h) and the ZnS@Cu-Zn cell (i) at the 1st, 50th, and 100th cycles.

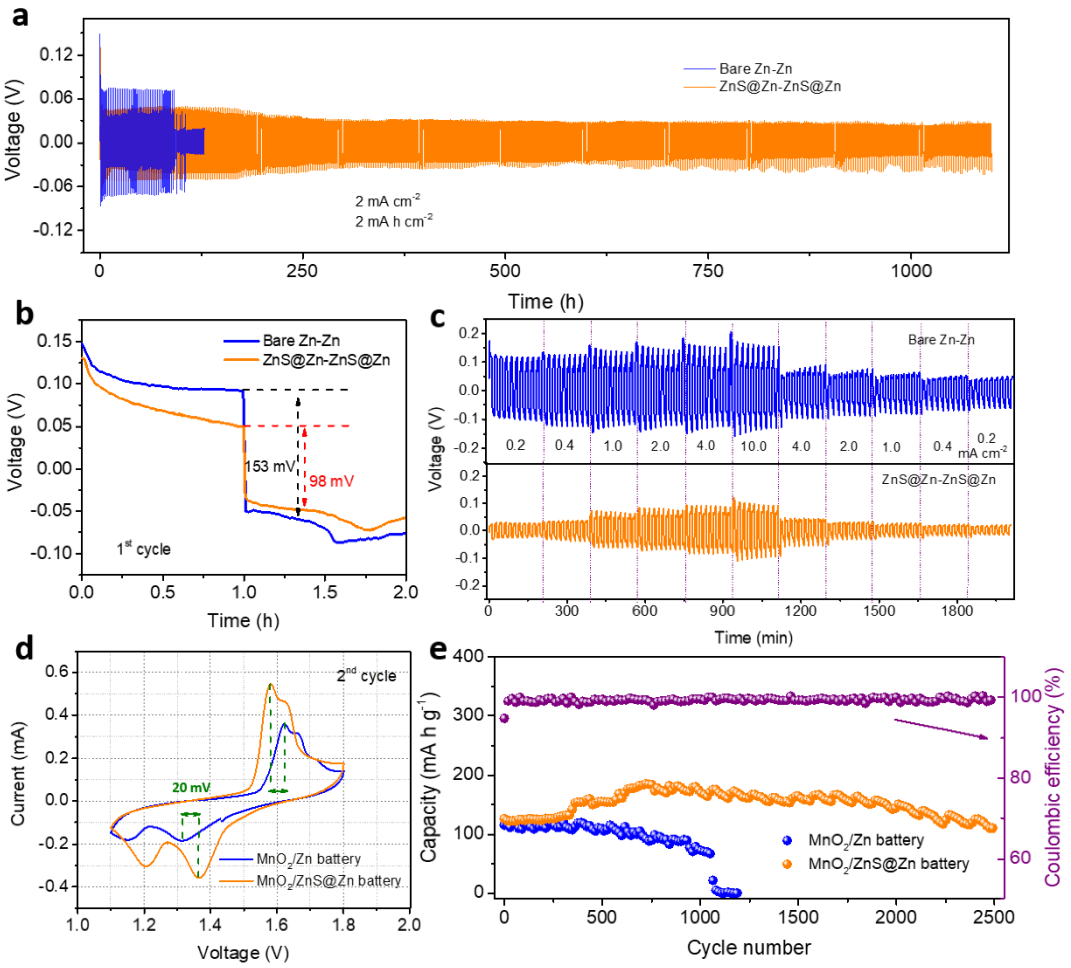

Figure 5. Electrochemical characterization of the samples. a) Comparison of the cycling stability of bare Zn and ZnS@Zn-350 in a symmetric cell at 2 mA cm^{-2} with the capacity of 2 mA h cm^{-2}. b) High-resolution voltage profiles for the 1st cycle. c) Rate performances of both cells at current densities from 0.2 to 10 mA cm^{-1}. d) Cyclic voltammograms for the 2nd cycle of MnO_2/Zn batteries using bare Zn and ZnS@Zn-350 anodes. e) Long-term cycling stability of both batteries at 5 C, along with the corresponding CEs (> 99.8%).

Based on the sulfur phase diagram, a dense and robust artificial layer of ZnS is introduced on the Zn metal surface via a in situ vapour-solid strategy. This ZnS protective layer not only suppresses the side reactions by blocking water from the Zn electrode surface, but also inhibits the Zn dendrite growth by guiding homogenous Zn plating/stripping.

Keyword: Zn ion battery

Junnan Hao, Bo Li, Xiaolong Li, Xiaohui Zeng, Shilin Zhang, Fuhua Yang, Sailin Liu, Dan Li, Chao Wu, Zaiping Guo*

An in-depth study of Zn metal surface chemistry for advanced aqueous Zn-ion batteries